

A comparison of synthetic aperture radars applied for satellite remote sensing of the ocean surface

David G. Tilley* and Yellepeddi V. Sarma**

*The Johns Hopkins University, Applied Physics Laboratory, Laurel, Maryland 20723-6099, USA. **National Institute of Oceanography, Physical Oceanography Division, Dona Paula, Goa, 403 004, India

ABSTRACT

Doppler imaging radars have orbited the earth aboard several spacecraft for the purpose of monitoring the ocean. Oceanographic applications of synthetic aperture radar (SAR) include measuring ocean wave fields, monitoring current fronts and sensing surface winds. The environmental interpretation of these remotely sensed ocean data is often restricted by incomplete understanding of SAR systems' capabilities and limitations. Hence, in this paper, the radiometric properties and spatial resolution of several SAR systems are compared based upon image data in sheltered bays and reservoirs. The upper limits of SAR system resolution in high sea states are discussed relative to wind and wave measurements made near hurricane Josephine with NASA shuttle imaging radar (SIR-B) aboard the space shuttle Challenger. The wave imaging capabilities of two more recent SAR systems, aboard the European ERS-1 and Russian Almaz satellites, over the Labrador Sea are observed in relation to an emerging consensus on Doppler imaging theory. The refraction and dispersion of surface gravity waves crossing the Gulf Stream were investigated by the NASA Seasat SAR in 1978 and again by the ERS-1 European SAR in 1991. Research results obtained during an international science and technology transfer project are presented as examples of ocean remote sensing applications.

1. INTRODUCTION

Surface wave dynamics is a branch of ocean physics that can be studied by probing the sea surface with radio waves (Phillips and Hasselmann, 1986). Phillips (1966) and others pioneered ideas on the equilibrium in wave action that balances wind stress with microscale breaking in steady sea states. Air-sea interactions have long been modelled as stationary and homogeneous point processes occurring at the Bragg wavelength of microwave

radiation backscattered toward radar remote sensors. The frequency of microscale breaking events, occurring during the time interval required for resolution of the Doppler coordinate, is important for understanding how a synthetic aperture radar (SAR) images the ocean surface. The concept of breaking wave frequency can be extended to include a random count of sea spikes in the radar cross section when the point scattering process is non-stationary.

The distribution and intensity of point processes (Karr, 1986) are subject to the statistical inference of probability laws in a stochastic system. A doubly stochastic Poisson process occurs when the mean density of Poisson random events is also a random variable. Hence, if a non-stationary point process is also non-homogeneous and subject to random clustering within its space, one can develop higher order moments of the point intensity in lieu of a clustering distribution. The radar concept of a uniform distribution of Bragg scattering wavelets can be maintained by summing moments of the Poisson random intensity when the transient point scattering process is also non-homogeneous. The phase of the Bragg clusters, with respect to gravity waves, remains a free parameter in SAR imaging models.

Scientific visualization (McCormick et al., 1987) is emerging as an educational tool for investigating relationships between theoretical models and empirical data. Visualization of is a form of communication that combines computer graphic concepts with image processing technology. SAR images of the sea surface are Fourier transformed to produce estimates of directional ocean wavenumber spectra. Stationary and homogeneous distributions of sea surface clutter are used to estimate the point response characteristics of spaceborne SAR remote sensors. Hydrodynamic distributions of localized surface discontinuities are modelled to simulate oceanic modulation of radar backscatter. Geometric tilt and velocity bunching

modulations of the radar cross section are used for theoretical inversion of the surface wave spectrum. The results of these modulation theories generate perspective plots of the surface that are shaded with the original SAR imagery to visualize correlations between surface texture and wave height.

1a. Ocean Applications of Synthetic Aperture Radar.

The NASA Seasat synthetic aperture radar (SAR) demonstrated a remote sensing capability [Beal, et al., 1981] for imaging surface wave fields, internal waves, air-sea interaction patterns and current boundaries. Of these features, SAR imaging of surface waves has received the most study and is consequently the best understood. The coherent and homogeneous modulations of radar backscatter by the tilt [Wright, 1968] and orbital velocity [Alpers et al., 1981] of ocean swell has been studied extensively with the assistance of Fourier statistics that characterize ocean wave fields in terms of wavelength and direction of propagation. The coherent velocity distribution of the sea influences the imaging of swell in a fundamental way that was quantified in terms of the range-to-velocity (R/V) ratio [Beal, et al., 1983] of the Seasat platform. The smearing of the wave image, due to Doppler broadening of the orbital velocity spectrum in high sea states, results in reduced along track resolution that is most evident in SAR image spectra as a band of wave power in the along track wave-number coordinate. However, the loss of wave-number response is partially offset by a commensurate increase in radiometric sensitivity to localized surface processes. The space Shuttle Imaging Radar (SIR-B) passed over hurricane Josephine in the North Atlantic Ocean aboard the space shuttle Challenger on October 12, 1984. Preliminary results of our analysis on the surface wave field spawned by the hurricane have been reported (Tilley, 1988) and a stochastic Poisson model of the SAR dynamic response to sea spike density and wind speed is a concept that should be developed in future SAR studies.

The SIR-B SAR also passed over Baie Missiquoi, a reservoir near Montreal in Canada, and its stationary response to sea clutter was compared to that of the Seasat SAR. Our stationary response analysis for the SIR-B system (Tilley, 1986) also included an optical model of Doppler imaging radars that points out similarities in the sampling statistics down range and along track, resulting from identical quadratic formulations of the coherent filters used for range-Doppler pulse compression. An on-board SAR processor has been designed at the Applied Physics Laboratory of The Johns Hopkins University for a future space shuttle mission (SIR-C), to produce ocean wave spectra (Beal et al., 1991a) from SAR signal data in real-time. These spectra will be compared with predictions of the U.S. Navy's global ocean wave spectrum models to assess the accuracy of computer forecasts and analyses.

The Johns Hopkins University Applied Physics Laboratory (JHU/APL) is currently involved in European Space Agency (ESA) and Office of Naval Research (ONR) managed programs to validate SAR data for global ocean research. We participated in a joint U.S.-Canada program to analyze European Remote Sensor (ERS-1) satellite data for SAR calibration and geophysical validation off the coast of Newfoundland. Nearly simultaneous and coincident SAR ocean imagery from the Russian Almaz satellite was also available at this site over the Grand Banks. The R/V ratio dependence in the coherent velocity bunching mechanism for surface wave imaging with SAR was investigated with the Grand Banks data set (Tilley and Beal, 1992) that also includes aircraft SAR and in-situ meteorological measurements of the surface wave field. We have reported (Beal and Tilley, 1992) SAR spectral ocean wave estimates from the ERS-1 SAR, operating over the Gulf Stream off the North American Continental Shelf. Current boundaries appearing in Advanced Very High Resolution Radiometer (AVHRR) images of the Gulf Stream, collected by NOAA satellites, will be compared with similar features in the SAR imagery.

1b. United Nations Development Program.

In 1991, a United Nations Program Grant was awarded to the National Institute of Oceanography located in Dona Paula, India. The Division of Physical Oceanography at the institute has applied funding from this grant to develop personnel and computer resources for oceanographic research. Scientists from each country have visited the other resulting in the transfer of ocean physics technology, image processing software and satellite radar data to the developing program. This project has been pursued jointly with JHU/APL located in the high technology corridor between the cities of Washington and Baltimore.

1c. Technology Transfer.

The Space Geophysics Group at JHU/APL maintains data processing systems to visualize relationships between radar data and air-sea interaction theories. Approximately 16 ocean scientists and remote sensing engineers are applying satellite data to geophysical research. Members of the group have been involved in oceanography with the synthetic aperture radars aboard NASA's Seasat and space shuttle platforms, satellite altimetry with the U.S. Navy's Geosat program, and atmospheric sounding and ship wake studies for the Department of Defense. Hence, specific software applications were developed for data analysis using a variety of different computer operating systems and a number of inherited hardware architectures. A local area Ethernet was developed to facilitate communication within the group and to allow efficient utilization of data acquisition, peripheral storage and display equipment.

The computer resources of the Space Geophysics

Group were linked as a node on the Applied Physics Laboratory Network Interconnect System (APLNIS) that connected other servers within the Space Department at JHU/APL to central communication resources. A Hewlett-Packard computer (HP-9000, Series 300) was used as the server equipped with a 1 Gigabyte (GB) hard disk, three 300 Megabyte (MB) hard disks and three 600 MB (i.e., double sided) optical disk drives. This server was equipped with two HP-7970 tape drives supporting 1600 and 6250 BPI (i.e., tape densities in bits per inch), a color HP-7550 pen plotter and a number of Laserjet and Postscript printers. The principal computational resource of the network (HP-9000, Series 700) was configured as a workstation with a 1 GB hard disk, a 5 3/4" CD-ROM (i.e., compact disc-read only memory) drive and a 600 MB double sided optical disk drive. Approximately eight IBM compatible computers, six Macintosh II computers and two Sun 3/60 computers were also configured as workstations. A Macintosh SE/30 computer was used to host a Kodak XL7700 thermal printer which is the principal device used for grey scaled and color image output of 8 1/2" x 11" prints and transparencies at 200 dots per inch. The Space Geophysics Group also operated a MicroVAX II computer equipped with a 300 MB hard disk, a 1600/6250 BPI tape drive and an Optronics C4300 color film-writer for 23 cm x 25 cm image formats at resolutions up to 400 lines per cm. Additional disk and tape drives were available at a remote site via APLNIS, a 10 MB/sec optical fiber network.

The group maintains internet services on its local area network and subscribes to electronic mail services provided by APLNIS. TCP/IP (i.e., Transmission Control Protocol/Internet Protocol) is the software protocol used for interconnecting the various hardware systems. The X-Window protocol is used to accommodate image and text displays at Macintosh and IBM compatible workstations for information computed with Interactive Display Language (IDL) software running on the HP 9000 computer. Specific application software was developed with the Fortran-77 language running under Unix-8 on the HP computers and VMS-5 on the VAX computers. A Macintosh computer was used to document research results. Adobe PHOTOSHOP and the IMAGE package, developed at The National Institutes of Health, were found helpful in addition to Microsoft word and other products marketed by Apple Computer, Inc.

In India, the National Institute of Oceanography's Physical Oceanography Division (NIO/POD) maintained a Microvax II computer under the VMS-5 operating system that was fully compatible with the VAX system at JHU/APL. Therefore, one principal objective of the scientists participating in the U. N. Development Program (UNDP) was to develop a computer software package at JHU/APL that could be transferred to NIO/POD for identical applications of

ocean physics technology at the two locations. Specifically, that software package was used to study surface wave fields appearing in SAR imagery by computing ocean wave spectra for ocean regions 6.4 km x 6.4 km square at many locations within much larger ERS-1 and Seasat data sets. Since both these sources of SAR data offer digital imagery on square 12.5 meter grids, the first requirement of the software was that it be capable of computing a two dimensional fast Fourier transform (FFT) over a 512 x 512 array of picture elements (pixels). This capability existed in the Interactive Display Language (IDL), a commercially available software package in use at JHU/APL.

The remaining requirements for SAR data processing software existed at JHU/APL in the form of Fortran programs running on both the UNIX and VAX computer systems. These programs applied linear models of the SAR stationary transfer function (STF), SAR dynamic transfer function (DFT) and the ocean-SAR modulation transfer function (MTF) to compute ocean surface wave spectra from IDL's two dimensional FFTs of SAR imagery. The Fortran programs for VAX systems were transferred from JHU/APL to NIO/POD on digital magnetic tape.

Id. Multi-Spectral Fusion of Chesapeake Bay Scenes.

The Chesapeake Bay estuary along the Mid-Atlantic Coast of The United States was imaged by synthetic aperture radar (SAR) systems aboard the European ERS-1 satellite in 1992, Soviet Almaz satellite in 1991, the U. S. Seasat platform in 1978, and by the thematic mapper (TM) optical system aboard the U.S. Landsat-4 platform in 1982. Landsat-4 and Seasat were free fliers at altitudes of about 700 and 800 kilometers, respectively, on November 2, 1982 and September 28, 1978 when they acquired imagery of the Chesapeake Bay. Almaz required active compensation for atmospheric drag which reduced its altitude from 294 to 283 kilometers between May 14 and May 22, 1991 when it acquired two scenes of the Chesapeake Bay region. The ERS-1 satellite imaged the Chesapeake Bay from an altitude of 780 kilometers on May 9, 1992.

A Chesapeake Bay bridge presented itself obliquely 40° from the SAR downrange coordinate, both for Almaz pass 822 and Seasat pass 1339. Almaz was descending with an inclination of 72.7° and Seasat was ascending with an inclination angle of 108°. Since the ground tracks of the descending Almaz orbit and the ascending Seasat orbit were within 1°, the Seasat track 334° from North was taken as the standard orientation for cylindrical projection to latitude and longitude coordinates. Multi-sensor fusion studies have been conducted to develop methods for registering Seasat, Landsat and Almaz satellite measurements. Control points, chosen at sea level, have been used to scale the SAR and TM data to a common map projection. The Landsat TM infrared (0.63 - 0.69 micrometers) image required rotation

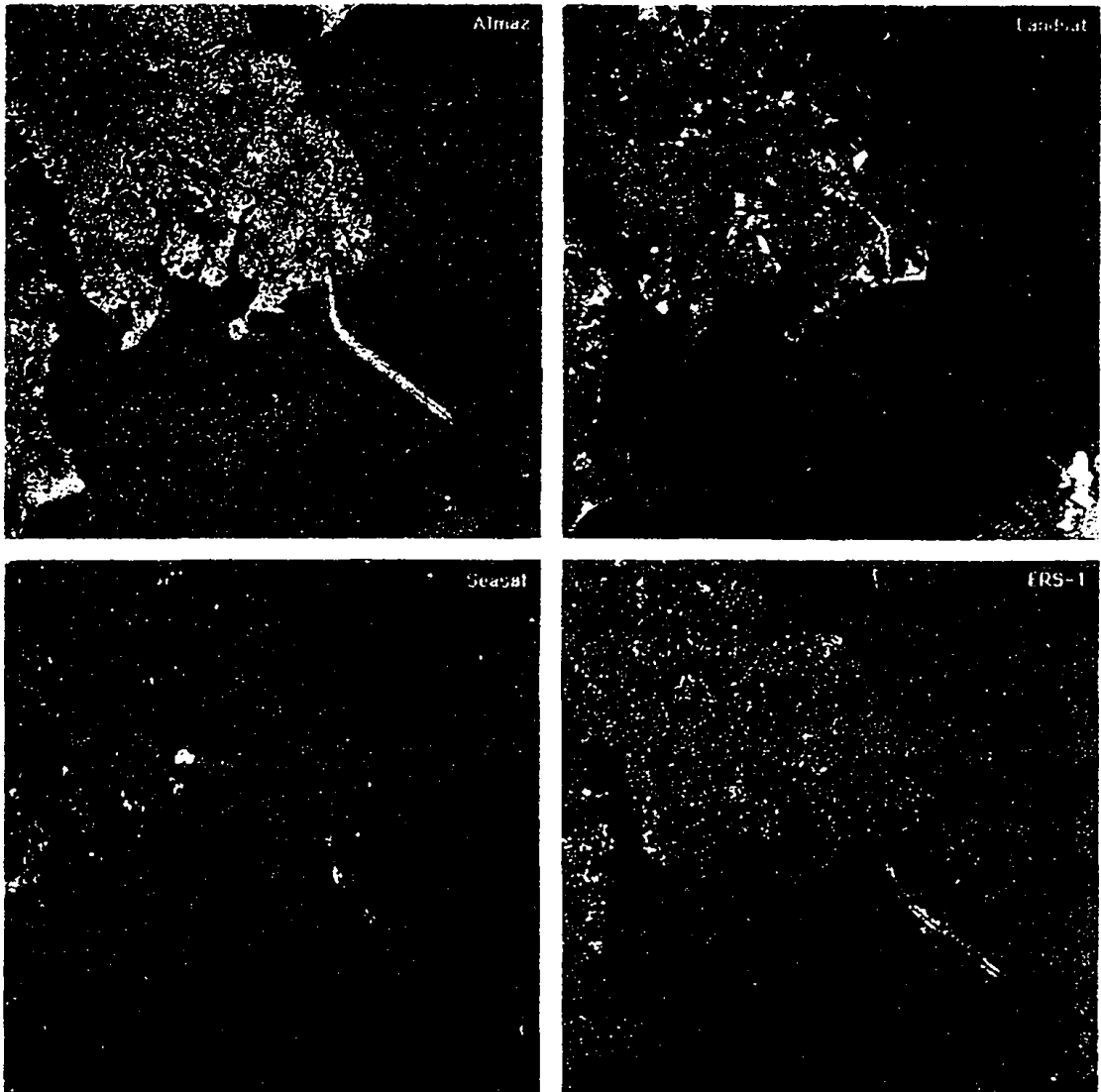


Figure 1. The Chesapeake Bay region was observed by the Almaz, Landsat, Seasat and ERS-1 satellites, respectively, on May 14, 1991, November 2, 1982, September 28, 1978, and May 9, 1992. The Almaz SAR image was created at NPO Machinostroyeniya in Moscow, Russia. Seasat SAR data were processed by the Jet Propulsion Laboratory under contract to the National Aeronautics and Space Administration. ERS-1 data provided courtesy of the European Space Agency (ESA®).

through 123° and scaling by a factor of 1.15 to map its 30 m/pixel data to the 25 m grid common to the Seasat data at 12.5 m/pixel and the Almaz data at 5 m/pixel. SAR image compression by pixel averaging has been applied to improve radiometric signal-to-noise properties for the Almaz S-band

(9.6 centimeters) and Seasat L-band (23.5 centimeters) data. Multi-spectral spatial correlation and coherence functions have been found effective in estimating the vertical elevation and horizontal separation of the twin spans of the bridge. Figure 1 depicts the multi-sensor data over a 14 km x 14 km

region that includes the Chesapeake Bay bridge

A Fourier domain fusion technique is defined as a statistical filter making use of two dimensional cross correlations between the optical and the SAR data sets. In the wavenumber domain $\{k_r, k_a: r, a=1, 512\}$, the Fourier transforms (\mathcal{A} , \mathcal{L} , and \mathcal{S}) of the Almaz, Landsat and Seasat images (A , L and S) are defined as

$$\mathcal{A}(k_r, k_a) = \iint A(r, a) e^{-ik_r r} e^{-ik_a a} dr da, \quad (1a)$$

$$\mathcal{L}(k_r, k_a) = \iint L(r, a) e^{-ik_r r} e^{-ik_a a} dr da, \quad (1b)$$

$$\mathcal{S}(k_r, k_a) = \iint S(r, a) e^{-ik_r r} e^{-ik_a a} dr da. \quad (1c)$$

Also, in the Fourier domain the SAR-optical correlation functions are defined as the cross conjugate (*) products

$$C_{\mathcal{A}\mathcal{L}}(k_r, k_a) = \mathcal{A}(k_r, k_a) * \mathcal{L}(k_r, k_a) / |\mathcal{L}(k_r, k_a)|^2, \quad (2a)$$

$$C_{\mathcal{S}\mathcal{L}}(k_r, k_a) = \mathcal{S}(k_r, k_a) * \mathcal{L}(k_r, k_a) / |\mathcal{L}(k_r, k_a)|^2. \quad (2b)$$

The mean values of these Landsat normalized correlation functions were computed and used to define a threshold equal to four times their product. The wavenumber domain was then segmented to equal the Fourier transform of the Landsat image where $C_{\mathcal{A}\mathcal{L}}(k_r, k_a) * C_{\mathcal{S}\mathcal{L}}(k_r, k_a)$ was greater than the threshold, the Fourier transform of the Seasat image where $C_{\mathcal{S}\mathcal{L}}(k_r, k_a)$ was greater than its mean, and the Fourier transform of the Almaz image where neither of the previous hierarchical segmentations applied. Fusion of the multi-sensor imagery

$$LSA(r, a) = \iint \mathcal{L}\mathcal{S}\mathcal{A}(k_r, k_a) e^{ik_r r} e^{ik_a a} dk_r dk_a \quad (3)$$

was accomplished by inverse Fourier transformation of the segmented wavenumber domain, $\mathcal{L}\mathcal{S}\mathcal{A}(k_r, k_a)$.

The scenes of the Chesapeake region were initially registered on the basis of the four control points. However, final registration of the multi-sensor data was based upon spatial phase and amplitude matching computations that identified peak sensor correlations based upon 256 x 256 pixel regions. The unnormalized Almaz-Landsat correlation function, $C_{\mathcal{A}\mathcal{L}}(k_r, k_a) / |\mathcal{L}(k_r, k_a)|^2$, can be validated by observing the distance between parallel features in the correlation surface. This distance is found to be approximately 133 meters, the horizontal separation of the twin spans of the Chesapeake Bay bridge, as can also be estimated directly from the Landsat image.

A two dimensional Almaz-Landsat coherence function has been used to estimate the mean height of the bridge as 49 meters, based upon interpreting a mean range coordinate shift in image phase (Tilley et. al., 1992) as the SAR layover effect. The inverse Fourier transform of

their complex conjugate product yields the coherence function,

$$COH_{LA}(h, v) = \iint (\mathcal{L} * \mathcal{A} / |\mathcal{L}| * |\mathcal{A}|) e^{ik_r h} e^{ik_a v} dk_r dk_a \quad (4)$$

in the h, v coordinates. When the two-dimensional spatial coherence function was computed over the bay bridge, the location of its central peak was displaced 4 ± 1 pixels, in both the range and azimuth coordinates, from the location of the central peak in the coherence function computed for terrain near the city of Annapolis at sea level. The 4 pixel shift in the azimuth coordinate is possibly related to a SAR Doppler velocity vs. scene elevation characteristic which has been observed previously (Tilley, 1984 and Tilley and Bonwit, 1989) without any measurable shift of range coordinate location of the coherence peak. The 4 pixel displacement in the range coordinate location of the peak coherence translates into a 49 m estimate of the mean bridge elevation by direct application of the SAR layover effect. The ± 1 pixel width of the coherence peak is probably the result of spatial variation in the elevation of the bay bridge which rises quickly from both shores to its maximum height of 57 m.

Section II of this article presents satellite imagery of the Chesapeake region along the Atlantic Coast of the United States of America recorded over the last dozen years from the perspectives of three different SAR remote sensors. Spatial resolution for the ERS-1, Almaz and Seasat SAR instruments can be estimated from their response to the wind roughened and limited waters of the bay that serve as a stationary (uncorrelated both spatially and temporally) distribution of backscattering sources. The stationary transfer function (STF) characteristics of a fourth SAR, the SIR-B system aboard the space shuttle Challenger, are also considered for a wind roughened scene of inland water sheltered from significant ocean swell. Section III of this article compares synthetic aperture radar scenes, recorded by the Almaz and ERS-1 satellites on May 23, 1991, of ocean waves propagating over the Grand Banks region off the coast of Newfoundland. The dynamic response characteristics of the two SAR systems are discussed in relation to the coherence of the matched Doppler filter used in azimuth compression of the single look Almaz and six look ERS-1 imagery. SIR-B scenes of hurricane Josephine are also included in the discussion of the SAR dynamic transfer function (DTF) model along with its relation to wind speed and sea spike densities. Section IV of this article describes the linear model of surface wave imaging with SAR and includes discussions of tilt, velocity bunching and hydrodynamic imaging mechanisms. The ocean-SAR modulation transfer function (MTF) is applied as the Fourier domain representation of the imaging model for directional estimates of ocean wave spectra. Surface

wave fields imaged by the Seasat SAR system are analyzed to study changes in slope spectrum statistics across the Gulf Stream. The MTF is also used as a Fourier domain filter for producing perspective plots of the sea surface under the winds of hurricane Josephine that can be shaded with the original SIR-B imagery to visualize correlations between surface texture and wave height.

II. THE STATIONARY TRANSFER FUNCTION FOR SAR IMAGING SYSTEMS

The Chesapeake Bay serves as a homogeneous distribution of independent point scattering sources for observing the stationary instrument response of SAR remote sensors. SAR backscatter from the bay scene has been used to compare image resolution for the ERS-1, Almaz and Seasat instruments. A SAR image of the Baie Missiquoi reservoir located near Montreal, Canada serves this purpose for the SIR-B remote sensor. In these wind roughened waters sheltered from surface waves, SAR image resolution of random noise can be observed with no large scale correlations between the surface signal and the pulsed Doppler radar. Hence, the distributed point amplitude and frequency response of the SAR should be reduced only by the finite time-bandwidth limitations of the imaging system, to include both the remote sensor and ground processor. Both radiometric and spatial resolution are considered within this context.

Ila. SAR Resolution Statistics For Distributed Clutter.

The radar field scattered back toward the ERS-1, Almaz, Seasat and Challenger platforms is the result of many scattering interactions at the sea surface. Bragg-resonant scattering (Wright, 1966) is usually assumed as the primary process by which microwaves are returned from an ocean surface roughened by short gravity waves raised by the wind. At L-band, the Bragg scattering process involves surface wavelengths on the order of 25 centimeters, smaller than the SAR cell size by a factor of 100. Hence, point specular reflection (Winebrenner and Hasselmann, 1988) over surface facets tilted toward the radar can be achieved on an intermediate scale that broadens with the current trend from L-band to shorter wavelength C-band SAR systems. These specular points are surface areas smaller than radar cells or image picture elements (pixels), but large enough to maintain phase coherence over 10, 20, 30 or more Bragg wavelengths. Hence, the transient specular condition requiring normal incidence can be relaxed to include arbitrary slope distributions and semi-coherent patches of Bragg wavelets.

The intensity and distribution properties of SAR image pixels are of interest. To first order, the statistics of a fading random variable are adequate to describe the SAR scattering intensity (Ulaby et. al., 1986) and higher

order statistics are expected to address distribution properties over a neighborhood of SAR pixels. Hence, for the stationary and homogeneous point scattering process, the SAR cross section for a single look image can be described as a Gaussian white-noise process (Vachon and West, 1992) with a exponential distribution fully characterized by its mean value. The root-mean square amplitude for a SAR image composed of N independent looks will then be a chi-squared distribution with a variance-to-squared mean ratio,

$$R2 = N \Gamma^2(N) / \Gamma^2(N+1/2) - 1, \quad (5)$$

fully characterized by N and the gamma function Γ . Surface height and slope statistics are usually related to the radar amplitude squared (i.e. the radar cross section) for which the intensity variance-to-squared mean ratio is 1/N.

Spatial resolution for the SAR instruments can be estimated from its response to wind roughened and fetch limited waters that serve as a stationary (uncorrelated both spatially and temporally) distribution of backscattering sources. The mean image intensity can be computed for a square array of 512 x 512 pixels and subtracted from the sample. A fast Fourier transform can be computed for the sample resulting in a power spectrum,

$$PS(k_r, k_a) = [\sum_r \sum_a SAR(r,a) e^{-ik_r r} e^{-ik_a a}]^2, \quad (6)$$

of the SAR image in the range and azimuth coordinates, $r=1,2 \dots 512$ and $a=1,2, \dots 512$. A stationary transfer function,

$$STF(k_r, k_a: I+J \leq 4) = \sum_{i=0}^I (k_r)^{2i} \sum_{j=0}^J (k_a)^{2j} c(i,j), \quad (7)$$

is defined by the 15 coefficients $c(i,j)$ of the polynomial formed by limiting the series to even order terms with combined range and azimuth order less than or equal to eight. The stationary transfer function (STF) for the SAR image response to distributed clutter can be approximated by fitting the polynomial function to the power spectrum by linear regression over the range and azimuth wavenumbers, k_r and k_a . The linear regression is conditioned by minimizing the squared error function,

$$S2 = \sum_{k_r, k_a} [PS(k_r, k_a) - STF(k_r, k_a: I+J \leq 4)]^2, \quad (8)$$

by taking its derivatives with respect to each of the 15 unknown coefficients to generate a set of 15 equations, $\partial S2 / \partial c(i,j) = 0$ solved by the method of Gaussian elimination

(Beckett and Hurt, 1967). Minimization of S2 and R2 for SAR systems indicates relative improvements in stationary point response, spatially and radiometrically, respectively.

This first order statistical model of the SAR image intensity will suffice for independent identically distributed pixels and stationary scattering processes. However, sea spikes (Jessup et al., 1990) occurring over the ocean surface produce a transient component of the radar cross section that appears correlated with wind friction velocity. For a SAR, the coherence of the Bragg resonant condition within pixels is most important because it influences Doppler frequency resolution of the along track coordinate. Therefore, this topic must be reconsidered for high sea states.

11b. Chesapeake Bay estimates of ERS-1, Almaz and Seasat Characteristics.

The SAR scene of the Chesapeake Bay, recorded by ERS-1 along an ascending pass (orbit 4257) on May 9, 1992, consists of 8000 x 8000 pixels (i.e., picture elements, each an unsigned 16 bit integer) depicting approximately a 100 km x 100 km region. This SAR database contains regions of wind roughened water over a limited fetch north of the bay bridge and serves as an adequate reference image for the calibration of ERS-1 resolution characteristics. A 512 x 512 pixel array of multi-look detected (MLD) format produced at the Canada Center for Remote Sensing, Ottawa) image data representing a 6.4 km square was extracted from the database north of the bridge. The ratio of the pixel variance to squared mean ratio for this six look data segment was $R2=0.049$ consistent with root-mean-square (RMS) detection of random noise in a six look process. One would expect this ratio to be 0.042 for RMS detection of the SAR signal amplitude in a six look process (Vachon and West, 1992), as opposed to $1/N=0.167$ for detection of the SAR cross section. Hence, the MLD format represents the SAR signal amplitude and is proportional to the square root of the radar cross section (RCS).

The Almaz SAR image of the Chesapeake Bay depicted in Figure 1 was geometrically rectified at NPO Machinostroyenia in Moscow, Russia. These data were recorded along a descending pass (orbit 822) on May 21, 1991 and mapped to a ground range projection representing a region approximately 44 km x 40 km as a square array of 8427 x 7899 digital numbers. The geometric processing and its documentation were found to be very accurate when choosing control points for registering this Almaz SAR image with an earlier Seasat SAR image, as discussed above.

The Chesapeake region was also imaged along an

ascending pass (orbit 705) on May 14, 1991 by the Russian Almaz SAR and the data product purchased by JHU/APL consisted of 8000 x 5832 pixels (i.e., picture elements, each an unsigned 8-bit integer) in a slant range perspective. A ground range resampling algorithm (Tilley, 1984) was applied to convert this database to 8000 x 7200 pixels representing a region approximately 40 km x 36 km. The ground range resampling algorithm replicates pixels at the variable rate needed to conform to a cylindrical map projection. Hence, the distribution of the image amplitude remained unchanged during the resampling process.

A 512 x 512 pixel sample for a 2.5 km square was extracted from the Almaz 705 scene of bay water just below the bridge. The $R2=0.219$ value, computed for this bay sample, is consistent with detection (Ulaby et al., 1986) of the SAR image amplitude or intensity, $0.273/N$ and $1/N$ respectively, assuming either 1 look or 4 look Doppler compression of the along track coordinate. Although it is not known whether a multi-look detection process was employed at NPO Machinostroyenia, the 8-bit pixel amplitude has been confirmed proportional to the square root of radar cross section (private communication with Pavel Shirokov). Hence, the $R2=0.219$ value can be compared to 0.273 and 0.132 which would be expected for the fading noise of a completely independent distribution of image amplitudes in 1-look and 2-look RMS detection processes. Hence, Almaz radiometric resolution is consistent with the normalized Rayleigh variance of a single azimuth look ($N=1$) SAR process that has been spatially oversampled by a factor less than two.

Both the Almaz data sets for the Chesapeake region represent the SAR image amplitude as 8-bit integer pixels. However, the scaling of the square root of radar cross section within the 8-bit precision was much better for the slant range perspective (orbit 705) than the ground range perspective (orbit 822). Hence, the extra effort required in mapping the Almaz image to ground coordinates at JHU/APL resulted in a data set comparable to the ERS-1 SAR in radiometric response. For comparison, the 16-bit SAR pixel amplitude of a square 6.4 km segment of the ERS-1 Chesapeake Bay scene (orbit 4257) was scaled to an 8 bit integer representation. Figure 2 shows the histograms (i.e., number of SAR pixels for each 8-bit integer value) for the SAR amplitude distributions in the SAR samples, each a square array of 512 x 512 pixels.

The procedure for estimating the SAR stationary transfer function (STF) is outlined above in Eqs. 6, 7 and 8. For this purpose, two 512 x 512 pixel scenes from Seasat pass 1339 as well as two scenes from Almaz pass 822 were chosen from the Chesapeake Bay region. The pixel data were squared to represent radar cross section and the mean RCS was subtracted prior to the application of two-dimensional fast Fourier transforms. The Fourier

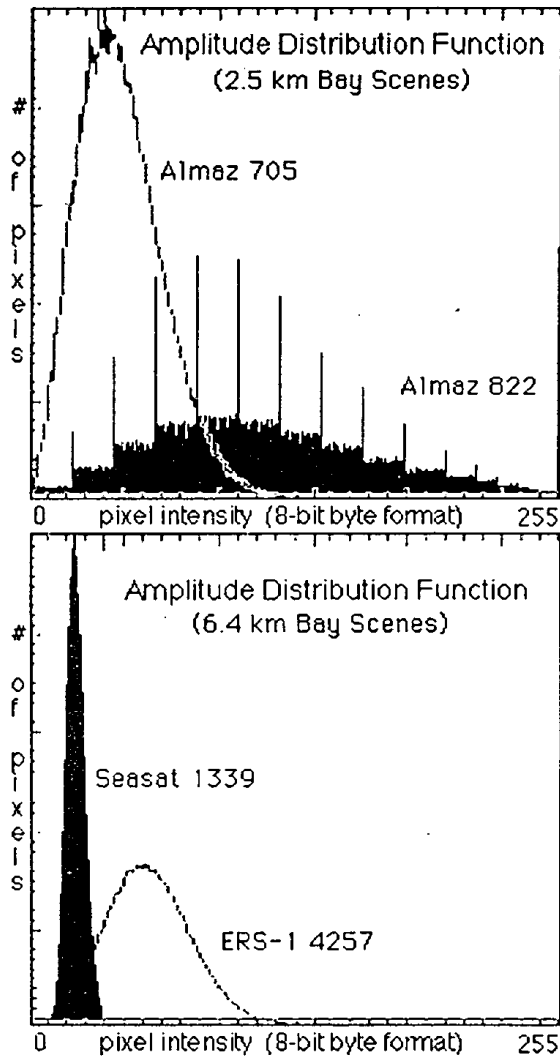


Figure 2. Histograms of Almaz (top), Seasat and ERS-1 (bottom) data show SAR amplitude distributions for sea surface clutter in the Chesapeake Bay.

power spectra resulting for each pair of Seasat and Almaz scenes were averaged to give the best spectral estimate of SAR spatial response to random sea clutter. Estimates of the polynomial trend function, $STF(k_r, k_a)$, that best fit the data were computed using Eq. 8 several times to include more or less of the data in the linear regression. During this process, the mean squared error could be used as a guide to select the best fitting STF function. The lower this error the better the fit. The 8th-order polynomials that

model the wavenumber response are defined by 15 polynomial coefficients that were later used to study surface waves crossing the Gulf Stream (Sarma, 1991). As discussed below in section IVb, SAR image spectra computed for the surface wave field over the Gulf Stream were corrected for the stationary wavenumber response of the Seasat instrument.

11c. Extending SAR Stationary Transfer Functions to Other Data Sets

In addition to the SAR systems aboard the Seasat, Almaz and ERS-1 satellites, the shuttle imaging radar (SIR-B) system was operated from the cargo bay of the space shuttle Challenger during October of 1984, approximately four months before its fatal launch and explosion over the North Atlantic Ocean. During that one week in 1984, Challenger flew over hurricane Josephine which presented itself in the North Atlantic Ocean as an unscheduled target of opportunity for observing high wind driven sea states with the SIR-B synthetic aperture radar. Table 1 compares some of the operational parameters of the SAR systems and their platforms.

SIR-B was a horizontally polarized L-band synthetic aperture radar processed on the ground with a four look Doppler filter to 25 meter resolution, similar in those respects to the Seasat SAR. However, the space shuttle platform was significantly different from the satellite platform in two important aspects. First, the space shuttle orbited at a much lower altitude so that the SIR-B range-to-velocity ratio was on the order of 35 seconds compared to 125 seconds for the Seasat SAR. This greatly reduced Doppler velocity smearing of azimuth travelling waves as will be discussed in section IV.

Secondly, the SIR-B incidence angle was variable from 15° - 60° , relative to Seasat's fixed incidence angle of 23° . Hence, the swath width and ground range resolution were variable. This latter effect arises during post-processing when the radar data are converted to a ground range coordinate from the slant range perspective in which

Table 1. SAR System Characteristics

Parameter	Seasat	SIR-B	Almaz	ERS-1
Satellite altitude(km)	800	225	300	780
Incidence angle(deg)	23	15-60	20-60	23
Pulse repetition(Hz)	1500	1280	3000	1680
Pulse length(μ sec)	100	30.4	33.4	37.1
Polarization	HH	HH	HH	VV
Swath width(km)	100	20-40	20-40	100
Radar wavelength(cm)	23.5	23.5	9.6	5.7
Surface resolution(m)	25x25	25x25	15x30	20x30
Number of looks	4	4	1	1, 3, 6

it was originally sampled. This geometric conversion (Tilley, 1984) is inversely proportional to the sine of the incidence angle. Hence, when a stationary transfer function is computed (Tilley, 1986) for the SIR-B operating at an incidence angle of 33.5° over a reservoir near Montreal, it can be used for correcting the SIR-B point response at other incidence angles by appropriate scaling

with the sine of the look angle ratio. This relationship should be kept in mind when using the contour plots in Figure 3 to compare the STFs for ERS-1 and Seasat at about 23° with the STFs of SIR-B and Almaz at about 33° .

The power spectral data used for constructing the STF polynomials for SIR-B pass 117.4 and Seasat orbit

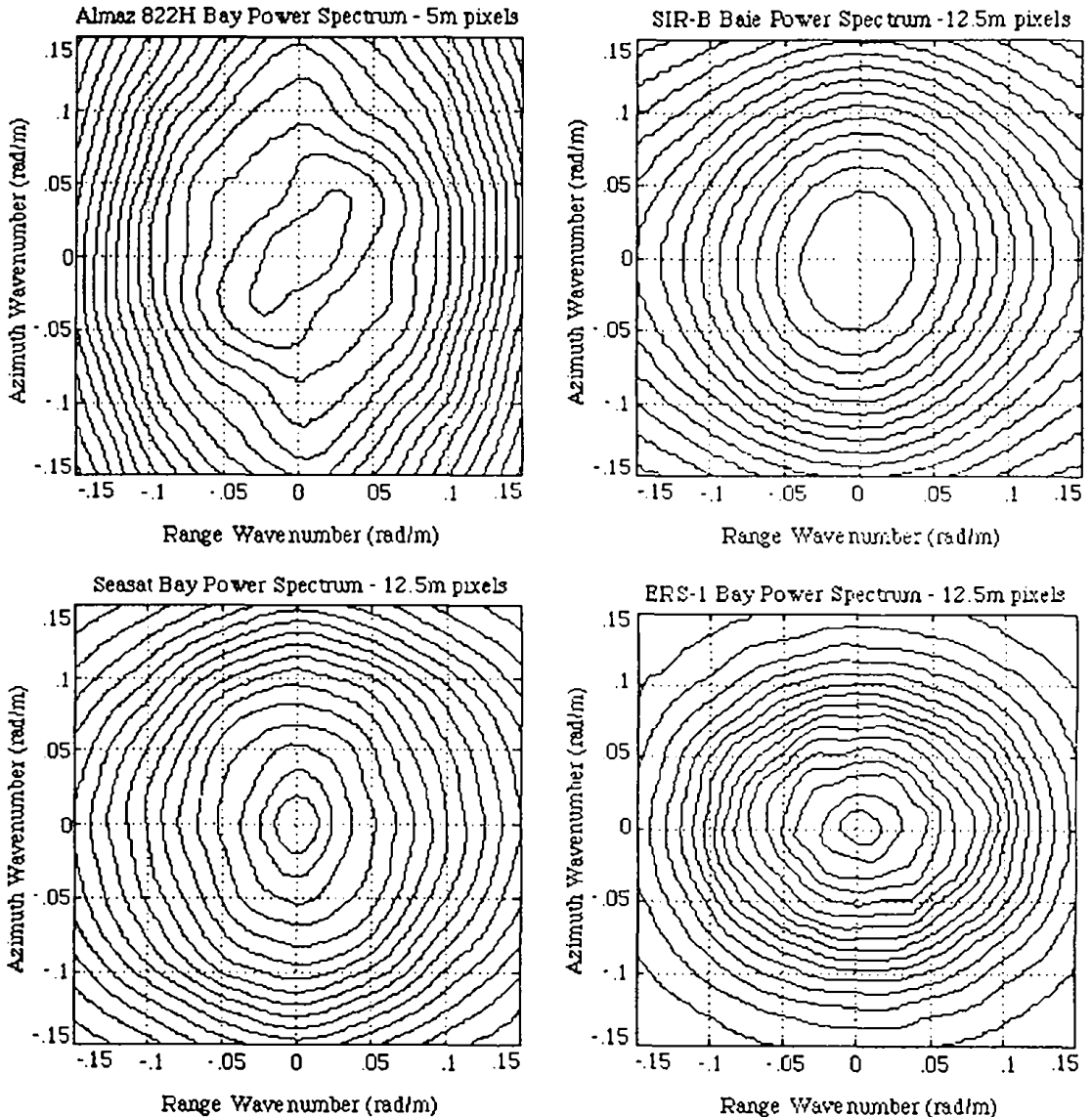


Figure 3 The SAR stationary transfer functions indicate is much better than the four look Seasat and SIR-B reduced spatial resolution on the same grid used by the

that the spatial resolution of the single look Almaz process systems. The six look ERS-1 system exhibits a somewhat United States of America SARs.

1339 are shown as two dimensional contour plots in Figure 3. Also shown are power spectra used to construct similar STF polynomials for Almaz orbit 822 and ERS-1 orbit 4257. The bay power spectrum for the Almaz image contained information out to wavenumber as large as $\pi/5 = 0.62$ radian per meter, whereas the other sensors have a common 12.5m grid and maximum wavenumber $\pi/12.5=0.25$ rad/m. The eighth of 16 equally spaced contours, only some of which appear within the 0.15 rad/m domain of Figure 3, is the half power estimate of an instrument's wavenumber response. This contour is located farthest from the origin for the single look Almaz spectra indicating greater wavenumber response and better spatial resolution.

The Almaz SAR was much like SIR-B in the two aspects discussed above. Furthermore, both radars employed horizontal polarization. The differences worth noting are that the Almaz space system employed a higher pulse repetition frequency and was compressed in Doppler frequency on the ground with one look rather than the four looks of the SIR-B. Hence, the Doppler partition and ambiguity suggest that radiometric quality is sacrificed for spatial quantity leading occasionally to bright object ghosts along track. The vertically polarized C-band ERS-1 system appears more sensitive than the horizontally polarized L-band systems to atmospheric disturbances of the ocean surface. This may be partly a result of the vertical polarization used by ERS-1, but it is worth noting that the Almaz scene of the Chesapeake Bay revealed subtle indications of surfactants and currents at S-band with HH polarization. Finally, ground processing support for ERS-1 offers many more options than any of its predecessors which will insure that a variety of applications develop for its data products.

III. THE DYNAMIC TRANSFER FUNCTION FOR SAR IMAGING SYSTEMS

The Gaussian concept of a homogeneous ocean surface characterized by a stationary wave spectrum may not be adequate for sea states that contain steep wavelets and breaking crests. Such surface conditions are characteristic of a developing sea in active generation due to wind stress resulting in so-called "spikes" in the radar cross section (Wetzil, 1986). These sea spikes exist as spatially localized discontinuities in the surface cross section that are transient in nature. The increase in sea spike contribution to real aperture radar cross section near nadir (Kwoh et al., 1986) is evidence that specular reflection adds a non-stationary component to coherent Bragg scattering. However, specular scattering from tilted surface facets need not be assumed to develop a non-homogeneous backscattering model. Broadening of the Bragg resonant interaction over coherent surface patches (Wright, 1966) was a part of the original scattering model

proposed to describe sea clutter. In general, the coherence of the radars' Bragg resonant interaction with capillary waves depends upon the spatial and temporal distribution of surface patches and their correlation with wind stress and wave phase.

IIIa. Exponential Decorrelation of Surface Backscatter

The scattering models applied to a SAR are much like those of a real aperture radar. Surface slopes that face the radar (facets) and coherent Bragg patches, existing on a scale intermediate between the radar resolution and radar wavelength, will contribute large amplitudes to the surface cross section instantaneously. A SAR differs from a real aperture radar in that its amplitude measurement is not instantaneous, but integrated over the time interval required for Doppler synthesis of the along track coordinate. When the cross section is dominated by sea spikes clipped in amplitude, the cross section measurement can be approximated by the number of point scattering processes occurring during the SAR integration interval. The mean rate M at which sea spikes occur per unit area A can be used to define the probability of counting m point processes per unit time. Furthermore the mean rate M at which these processes occur is known as the intensity of the point process (Karr, 1986) which is described by the Poisson distribution,

$$P(m; A, M) = e^{-M(A)} M(A)^m / m! \quad (9)$$

Clustering of point processes in the domain A can then be thought of as higher moments of the Poisson distribution characterized by its mean intensity M . For a SAR, the pixel area A corresponds to a range element, r , measured over a short time period and an azimuth element, a , measured over a longer time period (e.g., 0.001 seconds and 0.6 seconds, respectively for SIR-B). Technically, the mean sea spike density could be constant over the long time interval and a random variable over the short time interval in a doubly stochastic Poisson process. However, for a simple Poisson process, let $m=0,1,\dots,M$ be redefined as the order of the clustering distribution and K be the mean sea spike density along track to define the exponential autocorrelation function,

$$C(a) = C(a/2, -a/2) = \sum_{m=0}^M [e^{-K|a|} (Ka/2)^{2m} / m!m!], \quad (10)$$

for a SAR. Above, the zero crossing problem specific to SAR has been solved leading to the exponential form $e^{-K|a|}$ of the point intensity that is common to all the terms in the clustering distribution. For a real aperture radar without Doppler frequency filtering, the exponential forms cancel and the odd and even order linear terms alternate sign leading to an ordinary Bessel function (Tilley, 1988) useful

in the two scale model to describe the K-type distributions (Jakeman and Tough, 1988) now widely employed for statistical descriptions of radar data.

IIIb. Fourier Transform of the Exponential Correlation.

The space shuttle Challenger imaged surface waves over the Agulhas Current during the SIR-B mission in 1984. The SAR Dynamic Transfer Function (Irvine and Tilley, 1988) was developed as the Fourier transform of the Poisson exponential autocorrelation function,

$$DTF(k_a; K, M) = \int_{-\infty}^{\infty} C(a) e^{-ik_a a} da$$

$$= 4 \sum_{m=0}^M \left[\frac{(K/2)^{2m}}{(2m)! m!} \cos[(2m+1)\alpha] / \beta^{(2m+1)} \right] \quad (11)$$

where k_a is defined as the azimuth wavenumber and $\beta = (K^2 + k_a^2)^{1/2}$ and $\alpha = \arctan(k_a/K)$. In this model, the coherence of the Doppler frequency measurement of the along track coordinate is developed to order M for a clustering of discrete radar scattering events in terms of the radian wave density, or wavenumber K. The Fourier spectra for the surface wave field crossing the Agulhas were observed to be unusually high in amplitude, an effect partially attributed to an increase in transient backscatter produced by strong winds opposing the current. In this case, an order M=1 fit was preferred to the M=0 fit of the DTF to the slope variance spectrum estimated for swell enhanced by sea clutter. During the Labrador Sea Extreme Waves Experiment (LEWEX), progressively higher order models (e.g., M=1,2,3 and 4) of the DTF were found to best fit Fourier spectra (Tilley, 1989) for an aircraft SAR with progressively higher incidence angles (e.g., 10°-65°) across its ground swath. Hence, the non-homogeneous clustering of radar sea spikes appears to increase with sea state and also to increase with incidence angles closer to grazing.

The European Space Agency's SAR system aboard the ERS-1 satellite has imaged ocean waves over the Grand Banks of Newfoundland (Beal and Tilley, 1992) as part of a SAR calibration and validation experiment. On November 23, 1991 at 1414 GMT, the ERS-1 SAR obtained wave imagery over the Grand Banks (N46.5°, W51.0°) during descending orbit #1856. Approximately one hour later on that day (1520 GMT), a Russian SAR remote sensor aboard the Almaz satellite also obtained surface wave imagery over the Grand Banks ascending during orbit #3786. The wave spectra appearing in Figure 4 represent one six look ERS-1 image of dimension 6.4 km and the average of six single look Almaz images each of dimension 6.4 km. Hence, the incoherent noise-to-signal ratios of the SAR power data are nearly equal (e.g.

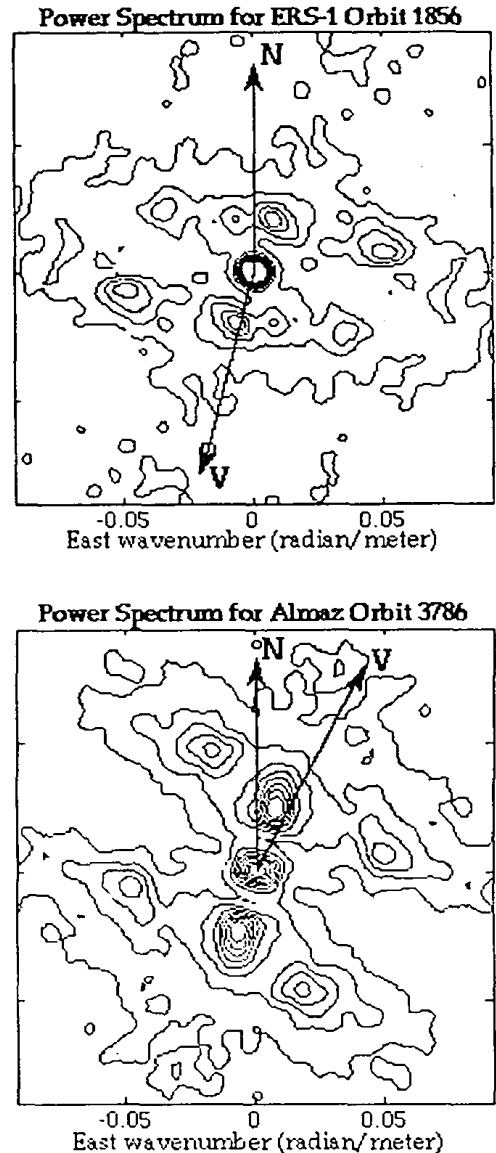


Figure 4. The azimuth wavenumber coordinates for the ERS-1 and Almaz SAR ocean spectra are parallel to their satellite velocity vectors, V, which are nearly opposite over the Grand Banks. Signatures of the north-south wave system are limited to an azimuth band that is narrower for the ERS-1 spectrum than for the Almaz spectrum.

1/6 following the discussion of Eq. 5) in this comparison of the spectra. These spectra have been rotated to orient North vertically and indicate an easterly swell propagating with a wavenumber of about 0.05 rad/m, equivalent to a

wavelength of about 125 m. The effect of reduced azimuth resolution is also evident for the southerly wave system. The taper of azimuth response in the azimuth SAR wavenumber coordinate, 13° from vertical (South) for the ERS-1 and 25° from vertical (North) for the Almaz spectra, is particular evident for the ERS-1 spectrum.

To address the resolution of the SAR azimuth coordinate within a 6.4 km square image, a single look Almaz spectrum must be compared to a six look ERS-1 spectrum. A 512×512 pixel ERS-1 power spectrum and a 640×640 pixel Almaz power spectrum, each corrected for its stationary transfer function, were averaged over the SAR range coordinate to produce one dimensional data characteristics for the azimuth taper. A speckle noise floor, equal to the mean spectral power divided by the number of azimuth looks (e.g., $\langle \text{psd} \rangle / 6$ and $\langle \text{psd} \rangle$ for ERS-1 and Almaz, respectively), was subtracted from the azimuth data characteristics.

Figure 5 depicts a basic difference in the Almaz and ERS-1 ocean data. The single look Almaz SAR results in higher spatial resolution (i.e. broadband or flat spectral response in azimuth wavenumber) but poorer radiometric resolution (i.e., large standard deviation in spectral power relative to its mean). The six look ERS-1 SAR results in lower spatial resolution (i.e., the severe azimuth taper) but better radiometric resolution characterized by a small noise-to-signal ratio. These observations are reflected in the empirical parameters found by regression of the DTF to best fit the azimuth spectral data. The upper wavenumber limit, K , was found to be larger for Almaz than for ERS-1 (e.g., 0.249 and 0.186 rad/m respectively) indicating better spatial resolution by improved Doppler frequency statistics (e.g., more sea spikes per pixel) over the longer single look integration time. The order of the clustering distribution, M , was found to be larger for ERS-1 than for Almaz (e.g., 4 and 0 respectively) indicating that random variations in the sea spike cross section were averaged over more Doppler time intervals for better radiometric resolution.

In general, the SAR cross section cannot be separated into its stationary and transient components. Hence, the coherent velocity smearing of the azimuth coordinate associated with velocity bunching is difficult to separate from the transient clustering of incoherent sea spikes that become blurred when averaged over several looks along track. In hurricanes, one might expect that both incoherent blurring of sea spikes and coherent smearing of velocity bunches would be maximized leading to poor wave images. Hurricanes Iva and Josephine, as imaged with the Seasat and SIR-B systems respectively, have been compared (Beal, et al., 1991b) demonstrating that the platform range-to-velocity ratio is the common factor limiting both types of azimuth response. Seasat and SIR-B

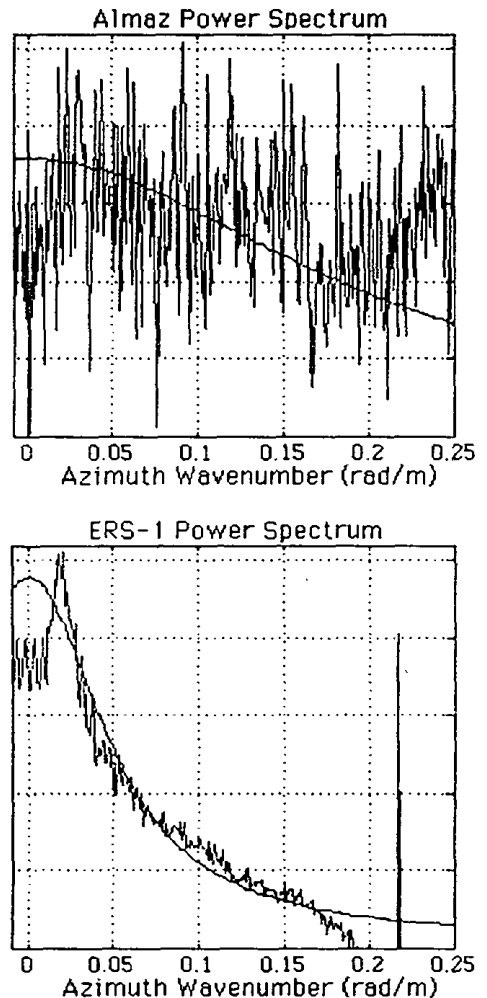


Figure 5. The azimuth travelling wave signal at 0.02 rad/m with an uncalibrated peak spectral power is more easily detected in the ERS-1 spectrum. The Almaz spectrum offers the possibility of detecting other wave systems at higher wavenumbers.

had a platform R/V ratios of 130 seconds and 35 seconds, respectively. Coherent velocity smearing limited Seasat SAR imaging of azimuth travelling waves to those longer than 300 meters, while the SIR-B SAR imaged waves as short as 200 meters. For the 6 meter sea states of hurricane Iva, the Seasat SAR broadband azimuth response (after correction for the DTF) was well below 100 meters and the SIR-B SAR broadband azimuth response approached 50 meters for the 9 meter sea states of hurricane Josephine. The broadband power that exists

in radar spectra may be the spectral signature of localized surface sea spikes (Jessup et al., 1990) whose number density and frequency are related to wind friction velocity.

IIIc. SIR-B's Correlation Statistics for Hurricane Josephine

Tropical storm Josephine reached hurricane strength on October 10, 1984 at approximately 30° N latitude and 70° W longitude in the Atlantic Ocean. Maximum sustained winds of 90 knots were reached on October 12 just 16 hours before the space shuttle Challenger carried the SIR-B synthetic aperture radar over the hurricane collecting image data for about 100 seconds covering an ocean swath approximately 650 kilometers long and 25 kilometers wide. This ground track lay north and east of Josephine at about a 45 degree angle to the storm track and came within 90 kilometers of the hurricane center at its point of closest approach. Digital imagery for this data take, AR-117.4, were obtained from NASA's Jet Propulsion Laboratory and partitioned into 100 square samples, each 512 x 512 pixels, representing 6.4 x 6.4 kilometers segments. These surface wave images were Fourier transformed into 100 estimates of the ocean wave spectrum to study the wave field spawned by the hurricane (Gonzalez, et al., 1987).

The 100 wave images have also been used to validate the Poisson exponential model of the SAR azimuth autocorrelation function. The SAR-optical spectral correlation function defined in Eq. 2a can be redefined as the cross conjugate (*) product of the SIR-B SAR image transform $S(k_r, k_a)$ with itself. In analogy with Eq. 3, the SAR autocorrelation function,

$$SS(r,a) = \iint S(k_r, k_a) \cdot S^*(k_r, k_a) e^{i k_r r} e^{i k_a a} dk_r dk_a \quad (12)$$

can then be obtained by an inverse Fourier transform of the SIR-B cross conjugate product. The result is a two dimensional correlation surface (Tilley, 1988) representing the point response function for the SIR-B scene. It was found that the range coordinate variation of the SIR-B impulse response function was well described by the stationary transfer function (STF) analysis of the Chesapeake Bay in the previous section, but that the azimuth coordinate response was broadened considerably by ocean wave dynamics.

A Doppler radar synthesizes the along track coordinate by compressing a time sequence of radar pulses within several individual looks. Point scattering processes that are distributed in time over the single look integration interval become distributed in the azimuth coordinate of the image. The point spread function is described by the exponential autocorrelation function $C(a)$ which can be compared to $SS(0,a)$. Such a comparison is presented in Figure 6 for one of the 100 image segments analyzed for

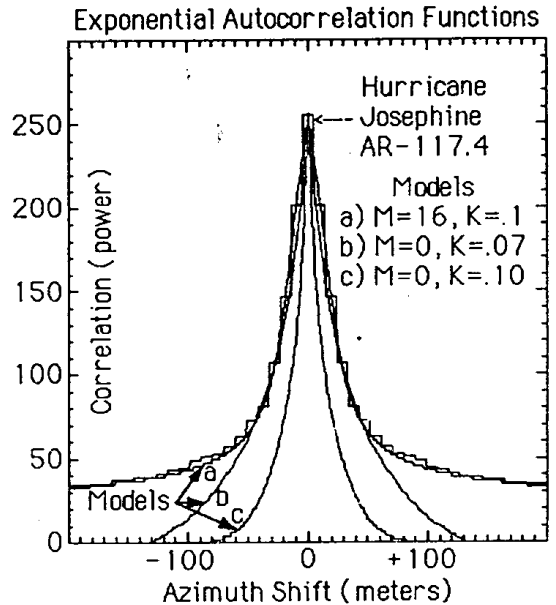


Figure 6. Purely exponential forms of the SAR autocorrelation function under estimate the azimuth point spread observed at low power in the hurricane Josephine data set. Higher order moments of the Poisson distribution accommodate the clustering of point scattering processes within the SAR integration interval.

SIR-B data take AR-117.4 near hurricane Josephine. The autocorrelation data, $SS(0,a)$, is depicted by the 32 power levels spaced at 12.5 meter increments across the azimuth axis. These data are well matched by the more continuous curve in Figure 6 representing C(a) computed from Eq. 10 with values of $M=16$ and $K=.10$ rad/m. The wave field was travelling in the range coordinate for this particular image and the azimuth point spread was quite severe requiring the high order autocorrelation function to match the low power broadening of the data distribution. A low order autocorrelation function ($M=0, K=.07$ rad/m), also shown in Figure 6, approximates the data profile by representing fewer point scattering events distributed more coherently in azimuth. The high and low order models agree on the half autocorrelation power estimate of spatial resolution, azimuth shift ≈ 40 m. The point spread function with order zero was found adequate for most of the 100 wave images when the waves were moving more obliquely to the radar look direction.

The Poisson model of Doppler pulse compression relates the coherence of radar cross section to an upper wave-number limit K on the SAR image spectrum. The SAR may be capable of sensing the equilibrium shape of the ocean wave spectrum in the saturation region where breaking waves are limiting growth. The procedure

involves modeling along track SAR resolution in terms of its upper wavenumber limit, K , with an exponential transfer function [Bendat and Piersol, 1971]

$$\text{DTF}(k_a; K, 0) = K/(K^2 + k_a^2) \quad (13)$$

that is fit by linear regression to the broad band azimuth component of the SAR image power spectrum, $\text{PS}(k_a)$, integrated over an appropriate band of range wavenumbers, k_r . In this fundamental model ($M=0$) of the SAR point scattering intensity, the theoretical amplitude of the short wave hydrodynamic modulation was found to be proportional to the square root of $\text{DTF}(k_a; K, 0)$ with K chosen to provide the best empirical fit to the SAR power spectrum for a number of SIR-B data sets [Tilley, 1987]. Implicit in this model is the assumption that short scale breakers are coherent with long wave slope variance [Monaldo and Beal, 1986] which is the statistic estimated in a SAR spectrum.

The close association between the upper wavenumber limit and the density of microscale breakers [Phillips 1985] suggests a new method for estimating the wind friction velocity, u^* . Microscale breaker density,

$$\Lambda = g_0^{-1}(k_1 \cdot k_0)^4 u^{*3} \quad (14)$$

has been related [Phillips, 1988] to the wind friction velocity u^* , where k_0 is the wave-number of the dominant surface wave, k_1 is the upper wave-number limit on its spectrum and g_0 is a constant that includes the gravitational acceleration. Wind friction velocity can conceptually be approximated by estimating the characteristic scale length, frequency and surface density of breaking waves. SAR may provide this information. SAR radiometric and azimuth response may indicate the frequency of microscale breaking in a wind generated sea where breaking waves are limiting growth. In this interpretation, radar cross section ($\sigma = \Lambda$) is a Poisson statistical sea spike density occurring with a Doppler frequency that results in an upper wavenumber limit ($K = k_1$) on SAR azimuth response. The SAR cross section is computed by summing the backscattered signal, clipped to 3-6 bits in amplitude [Curlander, 1986], over the aperture synthesis interval to produce a 16 bit intensity that is then reduced to 8 bits by taking the square root. The stationary component is well represented by this clipped amplitude, and Doppler processing merely integrates the homogeneous component of cross section over a small portion of the dominant wave period. However, the transient component of the backscattered signal results in a sum of equal amplitudes at the clipping threshold, so that the localized cross section degenerates to a mean Poisson statistical count of the breaking waves that produce the intermittent sea spikes. Assuming that transient backscatter component dominates

the stationary component in the high sea states of a hurricane, the third power of the wind friction velocity,

$$u^{*3} = g_0 \sigma (K - k_a)^{-4} \quad (15)$$

is related to the measured SAR cross section σ and the fourth power of the upper wavenumber limit K on the SAR spectrum, where k_a is the azimuth wavenumber of the dominant surface wave.

SAR wavenumber spectra have been computed over the 600 kilometer swath and used to hindcast the location of the storm track [Gonzalez, et al., 1987] from estimates of the wave velocity. Wind speed, U_{10} , estimates have been derived from an Ocean Data Gathering Program (ODGP) wind-wave model [Cardone, 1987] making use of all the available surface data. The SAR wavenumber response, K , and mean cross section σ were also estimated [Tilley, 1988] along the radar track as average values obtained from the four SAR image files nearest the latitude and longitude coordinates specified for ODGP model grid points. These data are listed in Table 2.

Table 2. SIR-B and ODGP Data

SAR and Spectral Statistics				ODGP Meteorology			
files	σ_0	K	k_a	lat	lon	U_{10}	H_s
	-	rad/m	rad/m	°N	°E	m/s	m
07-11	36.1	.0847	.0206	36.6	287.0	17.3	5.47
12-16	33.8	.0827	.0206	36.1	287.1	19.3	6.17
17-21	26.1	.0809	.0211	35.8	287.8	22.5	7.14
22-26	30.6	.0718	.0216	35.3	287.9	25.4	7.87
27-31	30.0	.0687	.0216	35.4	288.5	25.2	7.85
32-36	25.5	.0670	.0206	34.9	288.6	28.5	8.82
37-41	26.7	.0518	.0206	34.4	288.7	30.0	9.42
42-46	20.3	.0463	.0187	34.5	289.3	28.7	8.97
47-51	23.7	.0466	.0177	34.0	289.4	28.8	9.02
52-56	27.1	.0497	.0167	33.6	290.1	27.6	8.99
57-61	27.7	.0509	.0128	33.1	290.1	27.0	8.72
62-66	27.8	.0497	.0098	33.2	290.7	23.0	7.79
67-71	26.6	.0480	.0069	32.7	290.8	22.1	7.61
72-76	26.3	.0476	.0039	32.2	290.9	21.0	7.35
77-81	26.5	.0524	.0010	32.3	291.4	19.1	6.76
82-86	25.8	.0564	.0010	31.8	292.1	16.9	6.01
87-91	25.3	.0590	.0147	31.4	292.2	16.3	5.74
92-96	23.4	.0626	.0177	30.9	292.2	15.7	3.69

An optimal coefficient of proportionality for the SAR and ODGP data was determined by linear regression of the right hand side of Eq. 15 to the third power of the wind speed, U_{10}^3 , relating SAR cross section and wavenumber response to wind friction velocity. This coefficient, $g_a \sim g_0 (C_d)^{-3/2} = 0.00122$, includes the gravitational acceleration and the drag coefficient and would have had units of acceleration if the mean square SAR pixel value over the SAR integration time, σ_0 , had been calibrated in units of $m^{-2} sec^{-1}$. A SAR estimate of wind speed, called $u(\cdot) = (C_d)^{-1/2} u_{\cdot}$ in U_{10} units of m/sec, was then computed from Eq. 15 for comparison in Figure 7 with each of the 18 wind speeds used in ODGP.

IV. THE SAR MODULATION TRANSFER FUNCTION FOR WIND GENERATED WAVE FIELDS

The published work on ocean wave spectra using the SAR largely reports well developed ocean swell with wavelengths ≈ 200 m. Azimuth travelling wind generated waves in early stages of development are seldom detected in SAR imagery. The nonlinear aspects of the velocity bunching mechanism for imaging the sea are described (Krogstad, 1992) with a geometric series expansion of a coherent ocean-SAR spectral transform. Work on correcting the dynamic response of a SAR for coherent velocity smearing of the azimuth coordinate is in progress (Hasselmann and Hasselmann, 1991). In addition, the non-coherent backscatter from surface discontinuities is more significant for wind-waves than for swell waves. The reduced azimuth coherence of SAR backscatter also

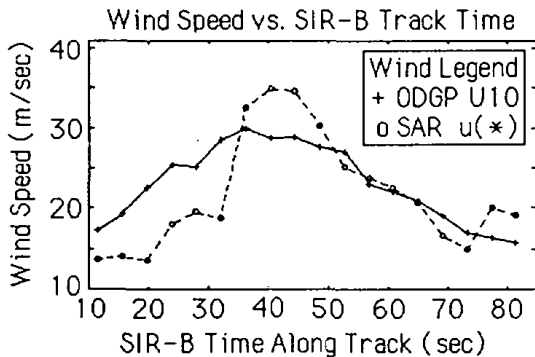


Figure 7. Wind speed is estimated from the SAR image cross section and the upper wavenumber limit on its spectrum. The kinematic wind speeds U_{10} from the ODGP model show a similar evolution over the SIR-B ground track passing about one day in advance and 100 kilometers ahead of hurricane Josephine.

results in a spectrum with reduced response at high wavenumbers. In section III of this chapter, the non-coherent backscattering transients that obscure the Doppler spectrum were modelled as an exponential series used to correct for the azimuth blur of SAR processors. Both of these processes are known as dynamic response correction, and it is possible that SAR imaging can be described as a sum of velocity bunching and hydrodynamic modulations addressable, respectively, with geometric series and exponential cosine models (Hogda et al., 1992).

IVa. Model of the SAR-Ocean Spectral Modulation.

A radar-wave modulation transfer function (MTF) can be applied to compute wave height and/or wave slope estimates for SAR image spectra. Our model of the MTF includes the effects of the tilt, hydrodynamic and velocity bunching mechanisms. The two-scale separation nonlinearities in the SAR imaging process are most severe for waves travelling in azimuth (Alpers, 1983). A Gaussian motion filter is employed along track to model advection of Bragg wavelets by the orbital velocity distributions derived from a Pierson-Moscowitz spectral distribution for wind-waves.

The Gaussian motion filter $G(k_a)$ can be modelled as (Monaldo and Lyzenga, 1986);

$$G(k_a) = \exp(-k_a/2k_\sigma)^2, \tag{16}$$

where $k_\sigma = (2\pi/3.93) (R/V)^{-1} (H_s)^{-1/2}$ rad/m; (R/V) is the range-to-velocity ratio of the satellite and H_s is the significant wave height. The tilt modulation (A_t), is the amplitude of Lyzenga's equation 4 (Lyzenga, 1987). The hydrodynamic modulation (A_h) and the velocity bunching modulation (A_v) are given by Monaldo's equations 5 and 6 (Monaldo and Beal, 1986). Then, a radar-wave modulation transfer function, MTF, is defined as

$$MTF(k_r, k_a) = [A_t(k_r) + A_h(k_r, k_a)] \exp(i\Delta_t) + G(k_a) A_v(k_r, k_a) \exp(i\Delta_v) \tag{17}$$

where, the phase factors Δ_t and Δ_v are defined relative to the radar look angle θ and wave angle $\phi = \arctan(k_r/k_a)$.

$$\Delta_v = \arctan(\sin\phi \tan\theta). \tag{18}$$

$$\Delta_t = \begin{cases} \pi/2 & \text{when } 0 < \phi < \pi, \\ -\pi/2 & \text{when } \pi < \phi < 2\pi. \end{cases} \tag{19}$$

The radar-wave modulation transfer function, MTF, in the above form gives wave slope spectra; for wave height spectra, the MTF can be multiplied by wavenumber, $k=(k_r^2 + k_a^2)^{1/2}$. Figure 8 shows sequentially a raw spectrum, a stationary response corrected spectrum, a dynamic

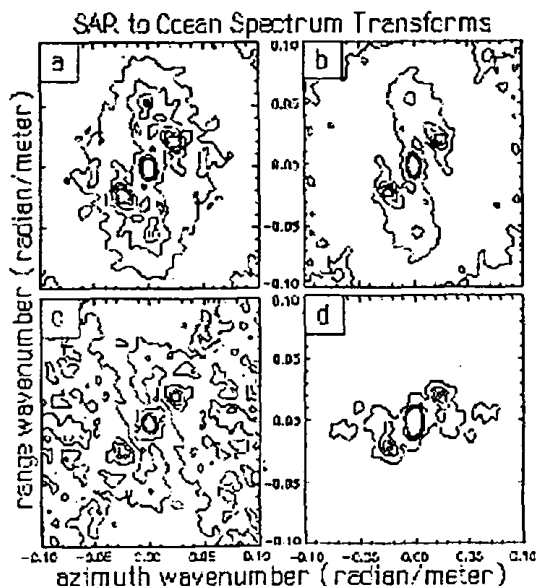


Figure 8. The Fourier power spectrum (a) of a SAR image is first corrected for the empirical estimates of (b) the stationary transfer function (STF) and (c) dynamic transfer function (DTF) of the Seasat imaging system. A modulation transfer function (MTF) based on theory is then applied to the SAR data spectrum for an estimate (d) of the ocean wave height variance spectrum.

response corrected spectrum, and a modulation transfer estimated height-variance spectrum. Throughout this sequence, there is a cluster of wave energy density at a wavenumber of 0.03 rad/m, approximately a 200 m wavelength, at an oblique heading relative to the radar axes. A secondary cluster of wave power in the azimuth direction becomes apparent at a wavenumber of about 0.06 rad/m, as the DTF and MTF operations are applied in Figure 8c and 8d, corresponding to a 100 m wavelength.

Ocean wave spectra are estimated by dividing complex SAR image spectra, $S(k_r, k_a)$ as defined in Eq. 1, by the amplitudes of the stationary and dynamic transfer functions $(STF \times DTF)^{1/2}$ and then by the magnitude of the complex modulation transfer function MTF. These spectrum processing operations are applied from 0 to $2\pi/25$ radian per meter, the Nyquist wavenumber for the Seasat 12.5 meter data. The resulting complex spectra are then detected as magnitude squared power spectra representing surface slope variance. Finally the spectra are smoothed using a discrete 15×15 (wavenumber) pixel approximation to a radially symmetric Gaussian kernel whose full width at half-amplitude is about 8 pixels. The smoothed spectra are related to unsmoothed spectra by equation 1 of Beal et

al. (1986). This process reduces the spectral density uncertainty and improves the statistical reliability of the spectral estimates. In each computer process the absolute value of the complex spectral amplitude is modified, rather than the Fourier power, to preserve the signal phase and conserve the signal power created in squaring pixel data to obtain the surface cross section.

IVb. Seasat Study of Waves Crossing the Gulf Stream.

The SAR imagery of the north wall of the Gulf Stream in North Atlantic Ocean was recorded during Seasat pass 1339 on September 28, 1978 at $35^\circ 45' N$ latitude and $74^\circ 28' W$ longitude. The motivation for the present study comes from the idea that the moderate surface winds measured by the scatterometer (SASS) might have been sufficient to generate the shorter wind waves (developing sea) which have not so far been reported for this particular data set (Beal et al., 1983 and Beal et al., 1986). In this context, it may be noted that Beal et al. (1986) did identify a less organized shorter wave system which they called "tertiary" wave system. They further stated that "... it is quite likely that the bulk of the energy from the tertiary system lies outside the narrow SAR response window and that the SAR is merely detecting that portion of the energy that happens to lie within its azimuth bandpass". We recently have improved the Doppler response model to account for the motion blur at high wavenumbers. Thus, an ocean study reported earlier by Beal et al. (1983 & 1986) was revisited to explore SAR data for spectral signatures of active wave development in the along track coordinate.

To examine the evolution of wave systems in this region, a set of 31 subscenes across the current boundary were chosen. Each subscene (512×512 pixels) is equivalent to an area of 6.4 km x 6.4 km. SAR image spectra computed from sets of four subscenes were then averaged to represent the ocean wave spectra for 12.8 km x 12.8 km frames. The squared image mean was calculated for each subscene and removed from the cross section. The data base was then fast Fourier transformed to produce two dimensional complex spectra. After correcting the Gulf Stream spectra for the stationary response of the instrument as estimated in the Chesapeake Bay, a uniform noise floor was subtracted from the spectra. The noise floor was estimated as the mean Fourier power at the highest azimuth wavenumber under consideration. The spectra were subsequently corrected for the dynamic wavenumber response of the instrument.

This dynamic transfer function, DTF, was given in Eq. 11 above. To begin the procedure, the Fourier power spectrum was averaged over the range wavenumber to yield a data profile as a function of azimuth wavenumber only. Then an error function,

$$D2(K,M)=\sum_{k_a}[DTF(k_a;K,M)-\sum_{k_r}PS(k_r,k_a)/STF(k_r,k_a)]^2, \quad (20)$$

was defined as the squared difference between the stationary response corrected power spectrum, PS/STF defined above by Eqs. 6 and 7, and the DTF. The azimuth power data profile was computed from the stationary response corrected spectrum by averaging the spectral data over all range wavenumbers greater than 0.010 and less than 0.125 radian per meter. The error function was evaluated for azimuth wavenumbers between 0.001 and 0.188 radian per meter. The dynamic model parameter, K, and the order of the model, M, providing the best fit to the input data were chosen to minimize this error.

In the earlier study, Beal et. al. (1983) reported a step change in the wavenumber of a 200 m swell system as it passed through the Gulf Stream. In the present work with the same Seasat data, we followed both a 200 m swell (primary system) propagating across the current and a 100 m wave system propagating nearly in the azimuth direction against the local current. We confirm the earlier observation including the statement that no refraction could be detected (nor expected) for this system as it approached and crossed the front perpendicularly. Note in Table 3 that the SAR power spectrum mean, $\langle S^2 \rangle$, decreased dramatically as the ocean swell passed across the north wall (i.e., moving from frame 7 to 8). This statistic correlates best with the location of the linear feature in the Seasat SAR image which can also be identified by the large variance-to-squared mean ratio (var) for the radar cross section in those frames. At the spectrum peak, the steepness $\langle s^2 \rangle$ of the primary wave system increased rapidly (i.e., moving from frame 6 to 7) about 6 kilometers to the interior of this north wall signature. The mean square surface slope, or steepness, is proportional to the wave slope spectral density integrated over wavenumber. Surface wave slope spectra were approximated by applying a modulation transfer function, Eqs. 16-19 above, to the SAR image spectra. The peak spectral density, or steepness $\langle s^2 \rangle$, we measured for the primary swell system increased in frames 1-7 and its wavelength (λ in meters) showed no discernable trend, so that its wave height may have increased as it approached the cold water front from inside the stream.

The azimuth travelling system appears to have been driven by northerly winds from cold water (frame 10) into the warm core (frame 1) of the Gulf Stream. This secondary wave system was deflected toward the East in the direction of the stream at the location of the north wall (frames 9 to 8) marked by a sharp decrease in the mean (ave) square image intensity. This wind sea was estimated steepest about 20 kilometers inside the north wall and was also its longest there (i.e., frames 5 to 3) with

Table 3: SAR Image and Spectrum Statistics for Gulf Stream Region.

SAR frame	Image		Spectrum		Primary Swell		Azimuth Sea	
	ave	var	$\langle S^2 \rangle$	$\langle s^2 \rangle$	λ (m)	θ	$\langle s^2 \rangle$	λ (m) θ
1	637	.235	4.63	0.64	226	298°	0.93	75 162°
2	713	.234	4.82	0.69	190	314°	0.97	102 157°
3	759	.233	4.96	0.67	205	291°	1.00	123 156°
4	797	.232	4.79	0.73	191	287°	1.04	122 148°
5	813	.232	4.83	0.78	205	295°	1.00	92 150°
6	850	.226	4.45	0.89	196	297°	0.92	80 160°
7	881	.236	4.23	1.13	192	296°	0.91	100 159°
8	980	.236	3.69	1.06	200	286°	0.91	101 149°
9	1234	.212	3.62	1.07	206	292°	0.94	87 152°
10	1364	.210	3.57	1.15	192	296°	0.95	70 155°

wavelengths decreasing by about a third on either side of this active region. Therefore, the azimuth wave system may have increased significantly in height, as well as in slope and length as it moved through this dispersive region. This secondary wave system also lurged toward the East ($\theta = 90^\circ$) as it passed through this active region.

When a wave train propagates into an adverse current, it becomes choppy and turbulent and as it passes further into a divergent stream the wave amplitudes decrease (Phillips, 1966). Our estimates also indicate that amplitudes increase as 200 m waves emerge from the stream. However, the 100 m waves exhibit increased amplitudes in dispersive regions of the stream. This may be a nonlinear wave effect or artifact in our SAR methods.

V. DISCUSSION

Va. Ocean-SAR Modulation Transfer Functions.

Velocity bunching modulation is an imaging mechanism caused by the apparent bunching in the along track position of Bragg resonant waves due to their advection by the orbital velocity distribution of an underlying ocean swell. However, the nonlinear dispersion and weak interaction between waves of different scales results in azimuth smearing of the apparent bunching of Bragg scattering sites in a SAR image. Hence, the nonlinear velocity bunching modulation exhibits a band pass characteristic in the SAR wavenumber coordinate along track.

Tilt modulation is an imaging mechanism that results directly from the geometric definition of cross section as the projection of the radar beam on the ocean surface at the incidence angle. The difference in the ERS-1 and Almaz SAR incidence angles, $23^\circ \pm 3^\circ$ and $42^\circ \pm 3^\circ$ respectively, at the Grand Banks site is an important

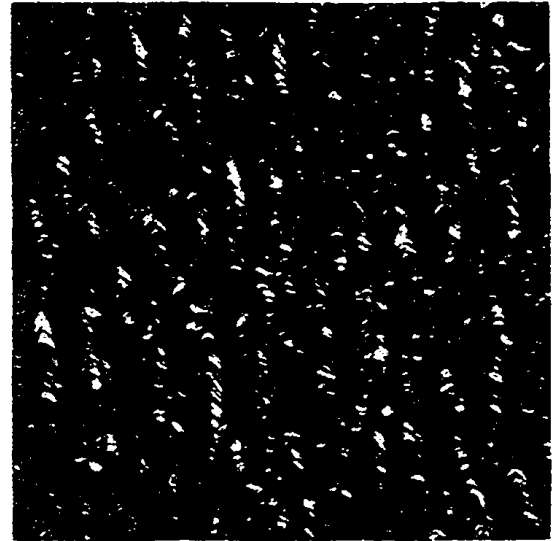
difference that favors ERS-1 for effective imaging of range travelling waves. However, tilt modulation also depends on polarization with the advantage going to Almaz's HH polarization over the VV polarization of ERS-1. The net ERS-1/Almaz tilt modulation ratio is less than 1.02 at the above incident angles. Seasat and SIR-B had the low incidence angle advantage of ERS-1 and the polarization advantage of Almaz.

Hydrodynamic modulation is an imaging mechanism that is poorly understood and generally considered insignificant in amplitude relative to the SAR velocity bunching and tilt mechanisms. However, experience with the Seasat and SIR-B remote sensors has shown that radar cross section statistics (Tilley, 1986) and SAR broad-band spectrum levels (Irvine and Tilley, 1988) are not adequately explained by Gaussian random speckle noise processes. Hence, it is possible that hydrodynamic modulation exists in relation to a transient component of the surface backscatter and appears similar to incoherent speckle noise during SAR data compression. Hydrodynamic modulation of Bragg resonant waves by long wave slope (Phillips, 1981) may be related to wind stress and microscale breaking as sources and sinks of the wave action spectral density.

Vb. Visualization of SAR Surface Topology

The shaded surface plot is a visualization tool that can be employed to gain a better appreciation of the relationship between the SAR modulation theories and the texture properties of the SAR imagery. The MTF involves two-scale interaction theory and the concept of long wave phase in the coherent modulation of short wave densities. Hence, the MTF is developed as a complex representation of the coherent sum of the tilt and velocity bunching modulations for the SIR-B geometry so that it can be applied to a complex representation of the Fourier spectrum computed for a square 6.4 km segment of the hurricane Josephine image. A noise floor is subtracted from the SAR data spectrum (Tilley, 1987) and a complex inverse Fourier transformation is applied to produce a filtered representation of the SAR image. If the MTF theories are valid and correctly applied, the filtered image represents an elevation map of the surface wave field that can be used to generate a three-dimensional contour plot using the IDL graphics package. Furthermore, the original SAR data can be used as texture information to lay a brightness distribution over the contour plot. Figure 9 was created using the IDL surface shading algorithm based on SIR-B data for hurricane Josephine.

This simulation depicts waves travelling toward the radar nearly perpendicular to the SIR-B ground track (i.e., shuttle velocity in the vertical direction). Breaking waves are apparent on wave crests. Bright patches found in wave troughs are thought to be foam from white caps



SAR look direction——> <----- Wind and wave direction

Figure 9. A perspective plot of SIR-B image data acquired near hurricane Josephine in the North Atlantic Ocean.

blown off their crests. Bragg wavelets may be generated on windward faces. Tilt modulation with -90° phase shift and velocity bunching with phase shifts approaching 180° were used in the MTF model. STF and DTF restorations reported in Sections IIc and IIc also were important in establishing a constant spectral noise floor that could be subtracted uniformly across the Fourier domain.

VI CONCLUSIONS

Vla. SAR Chesapeake Bay Calibrations

The Seasat, Landsat and Almaz scenes of the Chesapeake region have demonstrated the use of SAR and infrared optical sensors to determine horizontal and vertical separation of features common to both. Database fusion has been demonstrated for enriching the information content on a spatial grid reduced to a common 25 m sample size. Recent ERS-1 images of the Chesapeake Bay have been used to compare radiometric and spatial resolution characteristics with the Seasat and Almaz SAR systems. Conventional first order statistical models were validated by computing stationary transfer functions and signal-to-noise ratios for the SAR instruments' response to uncorrelated surface clutter in the bay.

Vlb. Hurricane Josephine Wind Speed Studies

SAR images of ocean waves generated under hurricane Josephine are remarkably well resolved for such a dynamical sea state. This suggests a hydrodynamic

mechanism assisting tilt and velocity bunching modulations. An exponential autocorrelation model, based on a Poisson statistical model of the SAR amplitude distribution, has been shown to agree with a SIR-B image data autocorrelation. Poisson model estimates of the azimuth wavenumber limit (Tilley, 1988) on the SAR ocean wave spectrum, combined with SAR measurements of mean cross section have been used to estimate wind speed according to Phillips' (1988) theory. These SAR estimates are well correlated with independent ODGP measurements of wind speed along the SIR-B track near the hurricane.

Vlc. Gulf Stream Current Studies

When a non-uniform current in the Gulf Stream region was included in their wave-current interaction model, Hayes & Shuchman (1981) found a refraction of waves due to the shear produced by wave-current interaction. Beal et al., (1986) observed a rapid change in the wavenumber of a 200 m swell system as it passed through the north wall of the Gulf Stream. If the Gulf Stream current is accompanied by considerable lateral shear (Phillips, 1981), the wave refraction effects would be significant, as observed above in Section IV for the 100 m azimuth travelling wave system. Although this wind sea spectrum was very poorly resolved, SAR spectral densities were observed above the speckle noise threshold for waves as short as 50 m. Although we observed these waves coming from the northwest, local winds were from the northeast. Hence, nonlinear velocity bunching effects may not have been fully corrected with our SAR imaging mode!

Vld. Grand Banks Experiment

Ocean waves are imaged in greater detail with the Almaz SAR, relative to the ERS-1 SAR, but with a larger variance in radar cross section that reduces statistical confidence in signal-to-noise thresholds. More of the Almaz and ERS-1 data, over the Grand Banks off Newfoundland, should be analyzed to investigate the roles of radar look angle and platform height-to-velocity ratio in SAR imaging of ocean waves. In addition; meteorological measurements and ship radar images and spectra, requiring hydrodynamic modulation modelling and inversion, are available at this site for validating a more complete SAR imaging theory. Such an understanding would be useful for designing future SAR systems and for assimilation of SAR and marine radar data into ocean wave forecast models.

ACKNOWLEDGEMENT

We are grateful for United Nations Development Program support, Goa Oceanographic Investigation Fellowships awarded for technology transfer by Shri. L.V.G. Rao at the National Institute of Oceanography and a Janney Fellowship awarded for documentation by The Johns

Hopkins University Applied Physics Laboratory. Portions of this work were supported by the National Aeronautics and Space Administration and The Office of Naval Research. We appreciate the assistance of P. Shirokov at NPO Machostroyenia in Moscow and of A. Scheffler at The Environmental Institute of Michigan for data documentation and software development. The ERS-1 SAR data were processed at the Canada Center for Remote Sensing under contract to the European Space Agency. Ocean Weather, Inc. provided the ODGP wind speed and wave height data for hurricane Josephine and we thank Vince Cardone for his kinematic analyses. We are also grateful for the helpful comments of R.C. Beal.

REFERENCES

- Alpers, W., P. B. Ross and C. L. Rufenach, J. Geophys. Res. **86**, 6481-6498, 1981.
- Alpers, W., J. Geophys. Res. **88**, No. C3, 1745-1759, 1983.
- Beal, R. C., P. S. DeLeonibus and I. Katz, Spaceborne Synthetic Aperture Radar for Oceanography, Johns Hopkins Univ. Press, 1981.
- Beal, R.C., D. G. Tilley and F. M. Monaldo, J. Geophys. Res. **88**, No. C3, 1761-1778, 1983.
- Beal, R. C., T. W. Gerling, D. E. Irvine, F. M. Monaldo and D. G. Tilley, J. Geophys. Res. **91**, No. C2, 2433-2449, 1986.
- Beal, R. C., S. F. Oden and J. L. MacArthur, Proc. of IGARSS'91, Vol. II, 443-446, Espoo, Finland, June 3-6, 1991a.
- Beal, R. C., T. W. Gerling, F. M. Monaldo and D. G. Tilley, Int. J. Remote Sensing, Vol. **12**, 1713-1722, 1991b
- Beal, R.C. and D.G. Tilley, Proc. of IGARSS'92, Vol II, 1325-1327, Houston, Texas, May 26-29, 1992.
- Beckett, R. and J. Hurt, Numerical Calculations and Algorithms, McGraw-Hill Book Company, New York, 82-94, 1967.
- Bendat J. S. and A.G. Piersol, Random Data: Analysis and Measurement Procedures, 56-98, Wiley-Interscience, John Wiley and Sons, New York, 1971.
- Cardone, V. J., Johns Hopkins APL Tech. Dig. **8**, No. 1, 24-32, 1987.
- Curlander, J. C., IEEE Trans. Geosci. Remote Sens. **GE-24**, 649-652, 1986.
- Gonzalez, F. I., B. M. Holt and D. G. Tilley, Johns Hopkins

- APL Tech. Dig. 8, No. 1, 94-99, 1987.
- Irvine, D.E. and D.G. Tilley, J. Geophys. Res. **93**, No. C12, 15,389-15,401, December 1988.
- Hasselmann, K and S. Hasselmann, J. Geophys. Res. **96**, No. C6, 10713-10729, 1991.
- Hayes, J.G and R.A. Shuchman, Oceanography from Space, J.F.R. Gower, Ed., Marine Series 13, Plenum Press, New York, USA, 469-476, 1981.
- Hogda, K. A., S. Jacobsen, H. E. Krogstad and G. Engen, Proc. of IGARSS'92, Vol. II, 1334-1337, Houston, Texas, May 26-29, 1992.
- Jakeman, E and R. J. A. Tough, Advances in Physics **37**, No. 5, 471-529, 1988.
- Jessup, A. T., W. C. Keller and W. K. Melville, J. Geophys. Res. **95**, No. C6, 9679-9688, 1990
- Karr, A. F., Point Processes and Their Statistical Inference, Marcel Dekker, Inc., New York, 1-39, 1986.
- Krogstad, H. E., J. Geophys. Res. **97**, C2, 2421-2425, 1992.
- Kwoh, D. S. W., B. M. Lake and H. Rungaldier, Proc. IGARSS'86, 319-326, Zurich, Switzerland, 8-11 Sept., 1986.
- Lyzenga, D.R., JHU/APL Tech. Digest 8, No. 1, 65-69, 1987.
- McCormick, B.H., T.A. DeFanti and M.D. Brown, Eds. Computer Graphics **21**, No 6, November 1987.
- Monaldo, F. M. and R. C. Beal, Wave Dynamics and Radio Probing of the Ocean Surface, O. M. Phillips and K. Hasselmann, Eds., Plenum Press, New York, 423-442, 1986.
- Monaldo, F. M. and D. G. Lyzenga, IEEE Trans. Geosci. Remote Sens., GE-22, 543-551, 1986.
- Phillips, O.M., The Dynamics of the Upper Ocean, Cambridge University Press, London, 59-60, 1966.
- Phillips, O.M., Spaceborne Synthetic Aperture Radar for Oceanography R.C. Beal, P. S. DeLeonibus and I. Katz, Eds., The Johns Hopkins Press, Baltimore, Maryland, USA, 24-31, 1981.
- Phillips, O. M., J. Fluid Mech. **156**, 505-531, 1985.
- Phillips, O. M. and K. Hasselmann, Wave Dynamics and Radio Probing of the Ocean Surface, Plenum Press, New York, 423-442, 1986.
- Phillips, O. M., J. Phys. Oceanogr. **18**, 1065-1074, 1988.
- Tilley, D. G., Electromagnetics **4**, 297-308, 1984.
- Tilley, D. G. , Opt. Eng. **25**, No. 6, 772-739, 1986.
- Tilley, D. G., Johns Hopkins APL Tech. Dig. 8, No. 1, 87-93, 1987.
- Tilley, D. G., Proc. of SPIE Conference on Statistical Optics **976**, 20-30, San Diego, California, August 18-19, 1988.
- Tilley, D. G. , IEEE Trans. Geosci. & Remote Sens. **27**, No. 5, 483-491, 1989.
- Tilley, D.G. and K.S. Bonwit, Remote Sens. Environ. **27**, 211-220, 1989.
- Tilley, D.G., Y.V. Sarma and R.C. Beal, Proc. of IGARSS'92, Vol. I, 665-668, Houston, Texas, May 26-29, 1992.
- Tilley, D. G. and R. C. Beal, Proc. of the 1st ERS-1 Sympos: Space at the Service of Our Environment, Vol II, 729-734, Cannes, France, Nov. 4-6, 1992.
- Ulaby, F.T., F. Kouyate, B. Brisco and T.H.L. Williams, IEEE Transactions on Geoscience and Remote Sensing Vol. GE-24, No. 2, 235-245, March 1986.
- Vachon, P. W. and J. C. West, IEEE Transactions on Geoscience and Remote Sensing Vol. 30, No. 3, 568-577, 1992.
- Wetzil, L., Wave Dynamics and Radio Probing of the Ocean Surface, O. M. Phillips and K. Hasselmann, Eds., Plenum Press, New York, 273-284, 1986.
- Winebrenner, D. P., and K. Hasselmann, J. Geophys. Res. **93**, No. C8, 9281-9294, 1988.
- Wright, J. W. , IEEE Trans. Antennas & Propag. AP-14, 749-754, 1966.
- Wright, J. W., IEEE Trans. Antennas & Propag. AP-16, 217-223, 1968.